

Ultra-high oxidation resistance of nano-structured thin films

E. Aschauer^{a,*}, T. Wojcik^b, P. Polcik^c, O. Hunold^d, M. Arndt^d, V. Dalbauer^e, P.H. Mayrhofer^b, P. Felfel^e, H. Riedl^{a,b}

^a Christian Doppler Laboratory for Surface Engineering of high-performance Components, TU, Wien, Austria

^b Institute of Materials Science and Technology, TU Wien, 1060 Wien, Austria

^c Plansee Composite Materials GmbH, 86983 Lechbruck am See, Germany

^d Oerlikon Balzers, Oerlikon Surface Solutions AG, 9496 Balzers, Liechtenstein

^e Department of Materials Science, Friedrich-Alexander-Universität Erlangen-Nürnberg, 91058 Erlangen, Germany

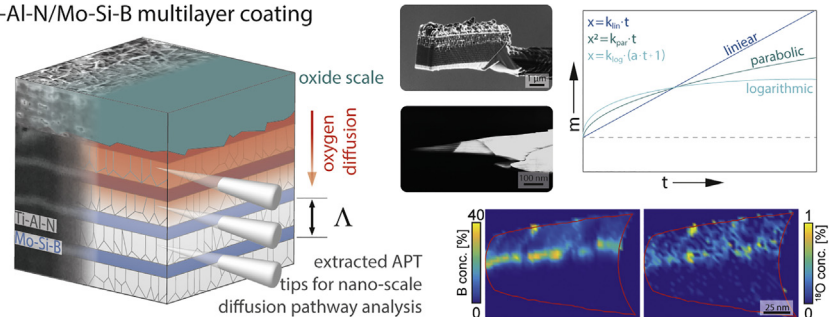


HIGHLIGHTS

- Ultra high oxidation resistance
- Blocking fast diffusion pathways through amorphous interlayers
- ¹⁸O tracer diffusion for highly resolved diffusion pathway analysis using atom probe tomography
- Identification of fast diffusion pathways in fcc-(Ti,Al)N protective coatings
- Atom probe tomography of nano-scaled (Ti,Al)N/Mo-Si-B multilayer coating.

GRAPHICAL ABSTRACT

Ti-Al-N/Mo-Si-B multilayer coating



ARTICLE INFO

Article history:

Received 22 September 2020

Received in revised form 13 January 2021

Accepted 15 January 2021

Available online 19 January 2021

Keywords:

Oxidation Mechanism

Ti-Al-N

Fast Diffusion Pathways

APT

Tracer Diffusion

ABSTRACT

Diffusion driven high-temperature oxidation is one of the most important failure mechanisms of protective thin films in industrial applications. Within this study, we investigated the diffusion of oxygen at 800 to 1100 °C through nano-laminated crystalline Ti-Al-N and amorphous Mo-Si-B based multilayer coatings. The most prominent oxygen diffusion pathways, and hence the weakest points for oxidation, were identified by combining ¹⁸O tracer diffusion and atom probe tomography. An oxygen inward diffusion along column boundaries within Ti-Al-N layers in front of a visually prevalent oxidation front could be proven, highlighting the importance of these fast diffusion pathways. Furthermore, the amorphous Mo-Si-B layers act as barriers and therefore mitigate the migration of oxygen by accumulating reactive O species at a nanoscale range. Preventing oxygen diffusion along column boundaries – through the implementation of amorphous interlayers – lead to parabolic oxidation behavior and stable scales even after 7 h at 1100 °C. Our results provide a detailed insight on the importance of morphological features such as grain and column boundaries during high-temperature oxidation of protective thin films, in addition to their chemistry.

© 2021 The Author(s). Published by Elsevier Ltd. This is an open access article under the CC BY-NC-ND license (<http://creativecommons.org/licenses/by-nc-nd/4.0/>).

1. Introduction

Diffusion driven transport mechanisms are crucial for various processes within materials and responsible for specific phenomena. Some prominent examples are recovery, recrystallization, precipitation hardening, as well

as phase transformations in general, but also complex procedures such as spinodal decomposition, nucleation and growth, or oxidation [1–6].

Diffusion is determined by parameters such as gradients in concentration (used for empirical Fick's first and second laws [2], although it is the chemical potential gradient that counts), electric fields, magnetic fields, elastic strain fields, or morphology (by providing fast diffusion pathways). Especially, oxide layer formation on metal surfaces is a textbook example for applying Fick's first law, describing the diffusion-controlled

* Corresponding author.

E-mail address: elias.aschauer@tuwien.ac.at (E. Aschauer).

scale growth. Tammann [7] mentioned the famous parabolic growth rate for scales on metals already in 1920. Later, the parabolic rate was derived from Fick's law by Pilling and Bedworth [8] parabolic law. Considering a simplified model (all metal oxides are of ionic nature), the transport kinetic and hence oxide scale growth are dominated by carrying metal cations or vacancies, electrons and holes, as well as oxygen anions (O^{2-}) [9,10]. If the formed oxide is non-volatile and effectively resistant to the transport of these specific species, the ongoing scale growth is restrained by the slowest transport process with respect to the reaction zone. A. Atkinson thoroughly summarized the fundamental mechanisms during oxide film growth of metal surfaces at elevated temperatures and highlighted the importance of the prevalent microstructure [11]. In particular, the diffusion along so-called short-circuit paths – e.g. grain boundaries, dislocations, or voids (extended defects) – is most significant if the temperature, T , is sufficiently below the melting temperature, T_m , following $T < 0.6 \cdot T_m$ [12,13]. Especially, the diffusion along grain boundaries was investigated in the past using atom probe tomography (APT) and tracer diffusion, highlighting their importance to describe the migration of certain species through a material [14–16]. In particular, the accelerated diffusion of oxygen along grain boundaries was shown for catalytic surfaces of Ir-Ru-O based materials [17]. This prerequisite is especially true during oxidation of Al and Cr containing protective coatings such as $Ti_{1-x}Al_xN$ or $Cr_{1-x}Al_xN$ forming Al_2O_3 and Cr_2O_3 scales, respectively [18,19]. Caplan and Sproule emphasized the important character of oxygen inward diffusion along grain boundaries [20]. Nevertheless, the interplay of the prevalent phases and amount of grain boundary interior with respect to the oxidation resistance of a protective coating is still discussed [21–23]. However, such coatings are typically applied in temperature regimes between 700 and 1200 °C, whereas in the so-called high temperature area (≥ 900 °C) the kinetics are highly accelerated and, hence, the oxidation protection is insufficient [24]. In addition, considering three stages [24] during oxidation – (i) transient stage, initial oxide formation of the available metals within a compound, (ii) steady state stage, diffusion controlled oxide scale growth, and (iii) breakaway oxidation, uncontrolled oxide formation of non-continuous scales – an in-depth understanding of the steady state regime is decisive for designing novel oxidation resistant coating materials. Especially, the interplay between stress formation (growth and thermal stresses) and prevailing diffusion processes (chemical depletion zones, similar to the Kirkendall effect [25]), but also the influence of voids and cavities along fast diffusion pathways still lacks experimental proof [9,26,27]. Here, the concept of oxide formation within a growing scale is relatively unexplored, and the local oxidation of grain-boundary interior within thin film materials exhibiting grain sizes in the range of 10 to 50 nm depicts still uncharted territory [10,15,28].

Therefore, we introduced a specific, nanostructured thin film to describe oxidation mechanisms along fast diffusion pathways (mainly column boundaries within thin films), see the schematics in Fig. 1a and b. The used multilayer coating is composed of highly crystalline layers, obtaining a well-known columnar morphology based on competitive growth during synthesis [29], as well as an amorphous laminate, only exhibiting very small nanocrystalline domains, as depicted in Fig. 1b. This concept features several positive aspects not only for a retarded scale growth itself, but also for a subsequent structural and analytical characterization of the morphology using high-resolution techniques. In principle, an array of crystalline and amorphous like layers depicts a strong barrier for diffusion driven processes, such as oxide scale growth, due to the annihilation of fast diffusion pathways [30–32] – see Fig. 1b. We therefore used our recently developed Ti-Al-N/Mo-Si-B multilayer coating (comprising alternating arc evaporated face centered cubic (fcc) structured $Ti_{0.57}Al_{0.43}N$ and magnetron sputtered amorphous $Mo_{0.58}Si_{0.28}B_{0.14}$ layers – see Fig. 1 [33]), which was proven to have unprecedented oxidation resistance [33–37]. In various isothermal but also dynamic oxidation treatments, the selected Ti-Al-N/Mo-Si-B multilayer coatings resist temperatures up to 1115 °C, before a complete breakdown emerges [38] (depicting a relatively high value with respect

to the chemistry and coating thickness [39]). Furthermore, the recurring nano-laminated architecture allows for excellent reference points during characterization, especially concerning the local grain boundary interior and thermal or chemical driven phase formations.

To trace oxygen diffusion pathways in such a nanostructured coating material, we initially used two different methods, each well-established for further characterization procedures, but rarely combined in such a manner. First of all, ^{18}O tracer diffusion, which is a well-known tool for describing diffusion pathways in oxide based materials such as perovskite typed electrolytes in fuel cells [40–43]. Through a combined conventional (^{16}O) as well as tracer (^{18}O) oxidation treatment, we preconditioned our growing scale, and consequently stain the predominant diffusion pathways.

In further consequence, to gain a sufficient spatial resolved chemical distribution (in the range of 1 nm or smaller), we used APT for a qualitative as well as quantitative analysis. Our present work provides an in-depth analysis of oxygen diffusion in a nanostructured Ti-Al-N based multilayer system by combining ^{18}O tracer diffusion with APT, highlighting the importance of an effective control and minimization of oxygen diffusion.

2. Materials and Methods

The multi-layered Ti-Al-N/Mo-Si-B coatings were deposited in an industrial scale Oerlikon Balzers INNOVA deposition system onto (100) oriented silicon, (-11; 02) oriented sapphire, and polycrystalline Al_2O_3 substrates as well as on low alloyed steel foil (which was subsequently dissolved in hydro chloric acid in order to obtain free-standing, flake-like coating material). The films were grown using powder metallurgically manufactured $Ti_{0.50}Al_{0.50}$ and $Mo_{0.50}Si_{0.30}B_{0.20}$ targets (Plansee Composite Materials GmbH). The alternating Ti-Al-N/Mo-Si-B architecture was realized by covering the respective sources with shutters. The $Ti_{1-x}Al_xN$ layers were arc evaporated in a nitrogen containing atmosphere (1000 sccm N_2 , purity 5.0) at a bias potential of -65 V, whereas the Mo-Si-B layers were sputter deposited in flowing argon atmosphere (500 sccm Ar, purity 5.0) at -40 V, respectively. Additionally, we also prepared an improved multilayer (with an optimized bilayer period), using a bias potential of -20 V and a reduced cathode current on the Ti-Al targets of 50 A during the deposition of the Mo-Si-B layers while keeping the other deposition parameters constant.

The substrates were carried by a two-fold rotating carousel (ca. 1.6 rpm) at a substrate temperature of 500 °C. Based on this process, a nanolayered architecture with a total bilayer period (Λ) of roughly 130 nm could be realized, comprising 16 bilayers with $\lambda_{Ti-Al-N} = 100$ nm and $\lambda_{Mo-Si-B} = 30$ nm – see also Fig. 1c to e. Further details on the coating synthesis can be found in [33,35–38].

The transport mechanisms of oxygen during high temperature oxidation in the nanostructured Ti-Al-N/Mo-Si-B multilayer system was analyzed by pre-annealing the coating in pure ^{16}O for 30 min in order to form an adherent oxide scale and subsequently aging in ^{18}O for 60 min at 900 °C. For cross-sectional bright-field transmission electron microscope (BF-TEM) and high-resolution TEM (HR-TEM) investigations, a 200 kV FEI TECNAI F20 S-TWIN TEM was used. For the cross-sectional TEM analysis, the coated Si substrate (as deposited state) was mechanically polished down to < 30 μm and subsequently ion beam milled to electron transparency, using a Gatan PIPS machine. In addition, the crystal structure was analyzed on a relatively small length scale using selected-area electron diffraction (SAED) and fast Fourier transformation (FFT). APT samples were extracted by a focused ion beam (FIB) lift-out in the as-deposited and oxidized state. However, the as-deposited APT specimens were obtained by using a keyhole technique [44], which places the analysis axis in the growth direction of the film. In contrast, due to weak film/substrate adhesion of the oxidized films which were deposited on sapphire, the oxidized samples were extracted perpendicular to the growth direction. This also allowed us to capture a larger area of the respective layers in the sample volume. To

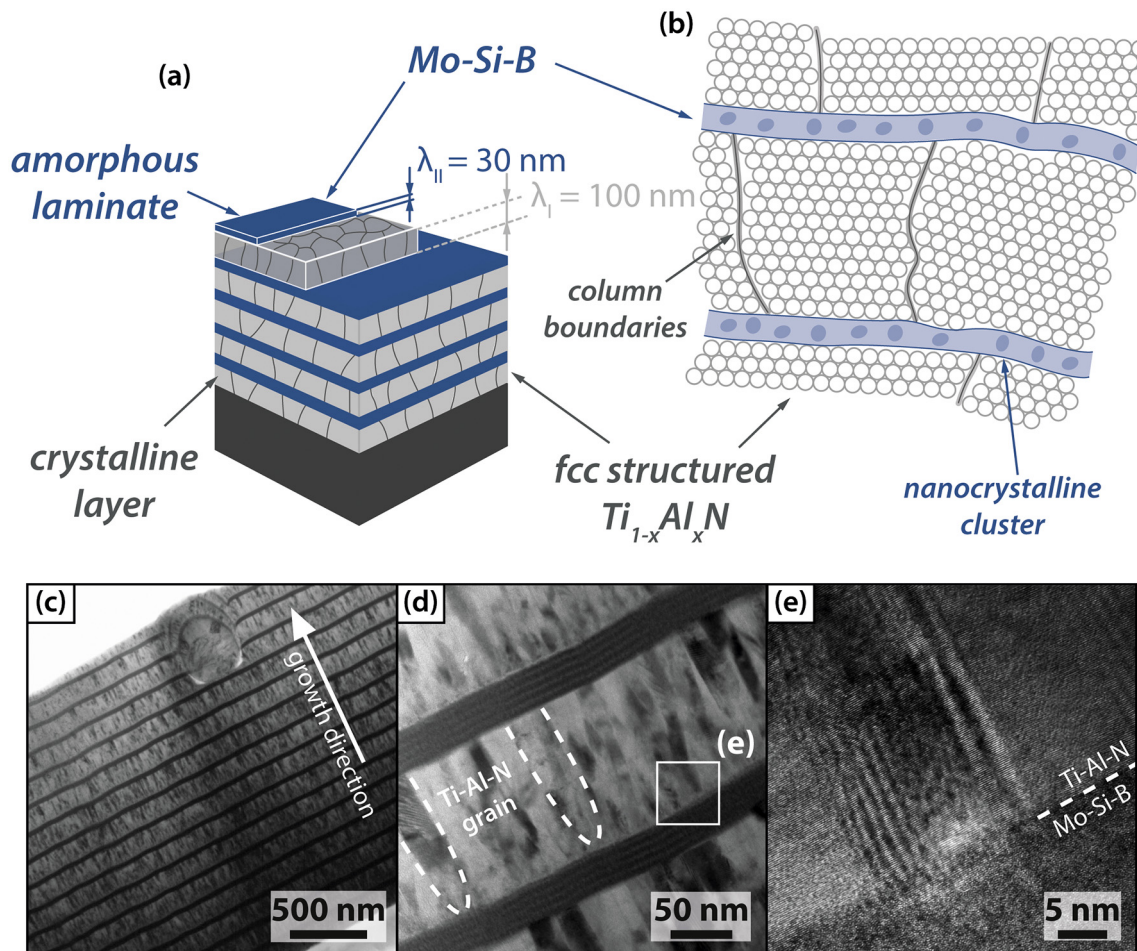


Fig. 1. Schematic description of the multilayer system, consisting of fcc-structured, crystalline Ti-Al-N layers as well as amorphous Mo-Si-B layers (a and b). The cross-sectional bright-field TEM (c and d) and HR-TEM (e) micrographs show the alternating stacked Ti-Al-N and Mo-Si-B layers in the as-deposited state, and reveal the V-shaped, crystalline nature of the Ti-Al-N layers, highlighted with dashed lines in (d). The inset in (d) gives the area for the HR-TEM image in (e).

investigate the diffusion of ^{18}O underneath the prevalent oxide scale for tracing the preferred pathways, three samples were taken at various depths (see also graphical abstract). All sample sharpening operations were undertaken at 8 keV ion beam energy, resulting in Ga damage free datasets [45], the Ga containing regions were discarded). The APT analysis was carried out on a Cameca LEAP 4000X HR in pulsed laser mode. This instrument is equipped with a 355 nm UV laser with a spot size of $\sim 2 \mu\text{m}$ and a reflection lens resulting in a detection efficiency of $\sim 37\%$. The experiments were done with a laser pulse energy of 50 pJ at a target evaporation rate of 1%.

During data set analysis, specific difficulties arise from the fact that some of the occurring ionic species share the same mass-to-charge ratio (m/c) [46]. For the consideration of the oxidation, this is most notably the main naturally occurring isotope of oxygen, ^{16}O , which e.g. overlaps with Ti^{3+} . Therefore, a conclusive analysis of the presence of ^{16}O before oxidation in ^{18}O is not possible. $^{18}\text{O}^+$ also shares its m/c with 1H_2 [16O^+ at 18 D, which can be present in small amounts as a contaminant during APT experiments from the sample transfer in the air. We therefore compared the presence of the 18 D peak in the data set from the as-deposited films to the oxidized material. This peak yield less than 0.02 at% in the Mo-Si-B layer in any of the as-deposited samples and is significantly higher than > 0.04 at% in the oxidized state at all height positions within the coating.

Finally, we derived specific strategies in order to improve the proposed coating architecture based on the findings of this study. The improved multilayer system was than investigated with respect to its

oxidation resistance by analyzing free-stranding coating material using a Netzsch STA 449 F1 Jupiter differential scanning calorimeter, especially focusing on the mass evolution due to oxidation. The samples were isothermally exposed to a mixed atmosphere containing synthetic air and He at temperatures of 800, 900, and 1000 °C for 7 h. An exclusively isothermal oxidation treatment was guaranteed by keeping the heating segment in inert He atmosphere. Additionally, we also oxidized selected multilayers under the same conditions on hard substrates (polycrystalline Al_2O_3 platelets) at 1000 and 1100 °C.

3. Results and Discussion

3.1. Structure, morphology, and chemical constitution

The coating consists of 16 bilayers in total with a uniform bilayer period of $\Lambda = 130 \text{ nm}$, see Fig. 1c and d. This architecture is divergent to the optimized coating thickness with respect to the oxidation resistance – based on our former studies – as well as the mechanical properties (consisting of 31 nm thin Ti-Al-N layers and 6 nm thin Mo-Si-B layers, [35]). Still, this coating architecture provides a stable and adherent oxide scale at 900 °C after 90 min, whereas Ti-Al-N of comparable thickness and chemistry is already fully oxidized after a similar oxidation treatment [24]. However, applying a significantly larger bilayer period tunes the architecture towards an optimized system for a detailed analysis of diffusion pathways by combining tracer diffusion experiments with APT analysis.

The Ti-Al-N layers crystallize in competitive growth as vertical, V-shaped columnar grains, as it is typically observed for PVD deposited thin films (highlighted by dashed lines in Fig. 1d) [47]. For this multilayer system, the morphology is strongly influenced by the incorporated Mo-Si-B layers, which force the Ti-Al-N to renucleate after each bilayer, see HR-TEM image in Fig. 1e. This limits on one hand, the crystallite size of the Ti-Al-N to the respective layer thickness (Fig. 1d) and suppresses, on the other hand, the evolution of continuous grain boundaries, ranging from the substrate to the top of the coating. An effective interruption of these structural defects depicts a crucial condition for a retarded kinetic of fast-diffusion pathway dominated oxidation processes. In contrast, the morphology of the Mo-Si-B layers appears mostly featureless, with no pronounced, oriented growth direction (Fig. 1d), nor defined long-range order (Fig. 1e), suggesting a nanocrystalline or even amorphous state. However, the repeatedly occurring, layered structured inhomogeneities within the Mo-Si-B layers are also indicated in Fig. 1d. These inhomogeneities are caused by the specific deposition process design. During the deposition sequence of the Mo-Si-B layer, the Ti-Al cathodes are kept running behind the shutters (and vice versa for the Ti-Al-N layers), in order to guarantee a stable synthesis process. Consequently, the double-fold substrate rotation also passes the shielded cathodes/targets, leading to this cross-deposition pattern (for more details see [33,38]). This effect is much more pronounced for the Mo-Si-B layers, since the deposition rate of the four Ti-Al cathodes is significantly higher than that of the two Mo-Si-B targets. Furthermore, the investigated coating system also exhibits incorporated macro particles (often referred to as droplets), which originate from the cathode during arc evaporation [48,49], see top area in Fig. 1c. However, usually the metallic droplets are also overgrown by the following layers, which helps to inhibit the oxygen inward movement along the coating material/defect interface. The elemental analysis and density evaluation of the APT data set within one Ti-Al-N layer suggests for an evenly distributed atomic composition, Fig. 2a. Consequently, we expect the material to be present as a homogeneous solid solution. The evaluation of a cross-contamination of the Ti-Al-N layer with impurities originating from the Mo-Si-B compound target is based on the

consideration of Mo, as Si and N share the same mass to charge ratio at 14 and 28 D [50]. Following this approach, we could find only a negligible contamination of Mo within the Ti-Al-N layer. A cut of the mass spectra, highlighting the presence of ^{18}O vs. $^{16}\text{OH}_2$ of the as-deposited state can be found in Fig. 4a (however, please note that the authors focused here on the quantification of the most important species rather than on a fully indexed mass spectra). Furthermore, a detailed analysis of the Ti-Al-N layer using HR-TEM (Fig. 2b) also confirms the nucleation of the Ti-Al-N crystallites on top of the incorporated Mo-Si-B layers. The corresponding FFT pattern (Fig. 2c) clearly reveals a single phased crystalline fcc structure (see marked area in Fig. 2b), showing a preferred 200 orientation in growth direction with no indications of the wurtzite AlN phase.

A detailed elemental cluster analysis of the APT data set of a Mo-Si-B layer (Fig. 2d) indicates an alternating occurrence of B and Al (and also Ti, not shown in the graph), which confirms the cross-deposition of Ti and Al during the synthesis of the Mo-Si-B layers. Additionally, a detailed HR-TEM analysis of a specific Mo-Si-B layer again reveals an amorphous-like appearance, showing no long-range order or crystalline clusters in (e).

This is also confirmed by the corresponding, blurred FFT pattern (Fig. 2f), which is a strong proof for an amorphous material (see marked area in Fig. 2e).

In summary, this detailed morphological and structural analysis confirms the proposed coating architecture and is the prerequisite for a proper interpretation of the oxygen tracer experiments. In addition, to rule out any thermally driven inter-diffusion between Mo-Si-B and Ti-Al-N, vacuum annealing experiments combined with HR-TEM and X-ray nano-diffraction proved an architectural integrity up to at least 1000 °C [51].

3.2. ^{18}O tracer experiments

In order to identify the most prominent diffusion pathways of oxygen during oxidation and hence the weakest points of such a columnar coating structure, we oxidized coated sapphire platelets at 900 °C in

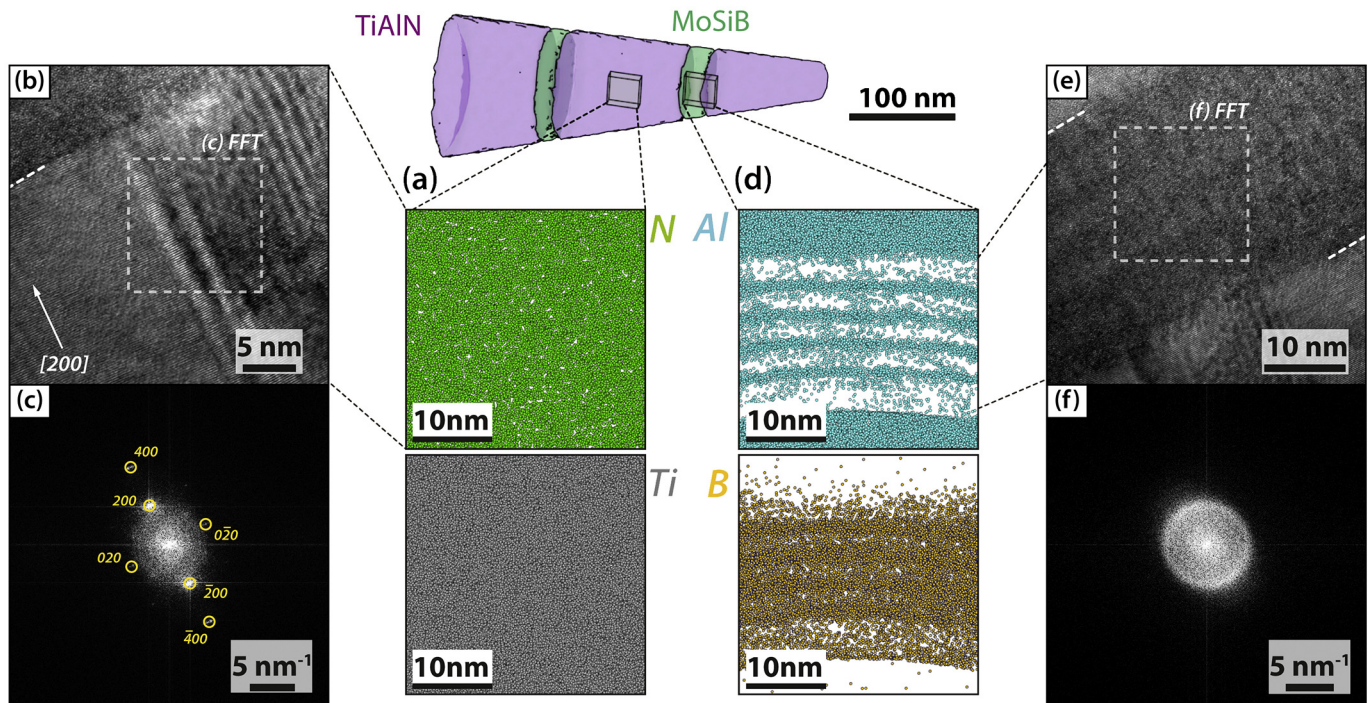


Fig. 2. Detailed APT analysis of a specific Ti-Al-N (a) and Mo-Si-B layer (d) in the as-deposited state, showing the elemental distribution of N and Ti as well as Al and B, respectively. The HR-TEM micrographs and the corresponding FFT of a crystalline, fcc structured Ti-Al-N layer (b and c) and of an amorphous Mo-Si-B layer (e and f) reveal the crystal structure of the two base systems. For preparational reasons, the analyzed sample volumes originate from different areas.

pure ^{16}O and subsequently ^{18}O atmosphere for 30 and 60 min, respectively. An overview of the formed oxide scale and a visually unaffected coating structure is given in Fig. 3a. The above described exposure leads to an oxidation of $0.65\ \mu\text{m}$ out of $2.2\ \mu\text{m}$ in total of the as-deposited coating thickness. The still intact coating morphology is covered by spacious Ti- and Al containing oxides, forming characteristic needle-shaped crystallites, which partially appear slightly undersense. Nevertheless, within this porous oxide scale, a kind of layered structure is recognizable – see Fig. 3a and c. Based on this visual inspection, the question arises if the prevalent oxygen partial pressure, either based on ^{16}O or ^{18}O , already causes a pre-oxidation or degradation of the grain boundaries underneath, being visually unaffected through the oxidation. Therefore, the oxygen distribution (especially the ^{18}O species) within the visually intact coating material was determined by preparing three APT specimens, extracted parallel to the coating/substrate interface, as illustrated in Fig. 3b. This was done by ion milling a free-standing slice, containing substrate, intact coating and oxide scale, see also Fig. 3c. An APT specimen ready for measurement, highlighting the parallel orientation of the layers with respect to the W post is shown in Fig. 3d. In Fig. 3e-g, a detailed chemical overview of the Ti-Al-N/Mo-Si-B interfaces is given, as obtained from the three different specimens, extracted from the oxide scale near region (Fig. 3e), within the middle regime of the unaffected coating (Fig. 3f), as well as from the substrate near area, Fig. 3g.

The mass spectra of the as deposited as well as oxidized states are presented in Fig. 4. Fig. 4a gives the mass-to-charge-state ratio of the

$\Lambda = 130\ \text{nm}$ in the as deposited state – corresponding to the results presented in Fig. 2 – whereas Fig. 4b to d correspond to the oxidized states as shown in Fig. 3e to g, respectively. To highlight the presence of ^{18}O in the oxidized state, but also to verify that the amount of $^{16}\text{OH}_2$ in the as deposited state is minor, we focused on the region between 8 to 20 Da. The amount of species arriving at 18 Da during APT is significantly higher for the oxidized states, whereas the intensities at 16 Da stays rather constant, compare Fig. 4a to d. The tip which was prepared nearest to the visually oxidized area (porous scale), see Fig. 3b and e, obtains a 5 times higher amount of species at 18 Da compared to the as deposited sample. The ratio of $^{18}\text{O}^+ / ^{16}\text{O}^+\text{H}^+$ is highest for the oxidized, surface-near sample (red tip), 4.50, and decreases with progressing depth of the sample position within visually unaffected coating to 2.96 for the middle (green tip) and 2.30 for the bottom tip (blue one, substrate-near position), respectively. In the as deposited state the ratio between $^{18}\text{O}^+ / ^{16}\text{O}^+\text{H}^+$ is 0.80. In summary, the tips of the middle and bottom section – see Fig. 4 c and d corresponding to Fig. 3f and g – still have significant higher amounts of species at 18 Da. Nevertheless, all data sets in Fig. 3e to g of the respective specimens are cropped in the same way, that a full Ti-Al-N/Mo-Si-B bilayer is displayed, where the ^{18}O atom distribution (blue colored dots, left side) is compared to the B atom distribution (yellow colored, right side). Based on this selection, an interdiffusion of the two layered coating materials as well as preferred diffusion pathways are distinguishable. For all three specimens, the B atoms allow for a sharp distinction between Ti-Al-N (nearly B free, left side) and Mo-Si-B layers (B containing, right side). In addition, for all specimens, the ^{18}O amount

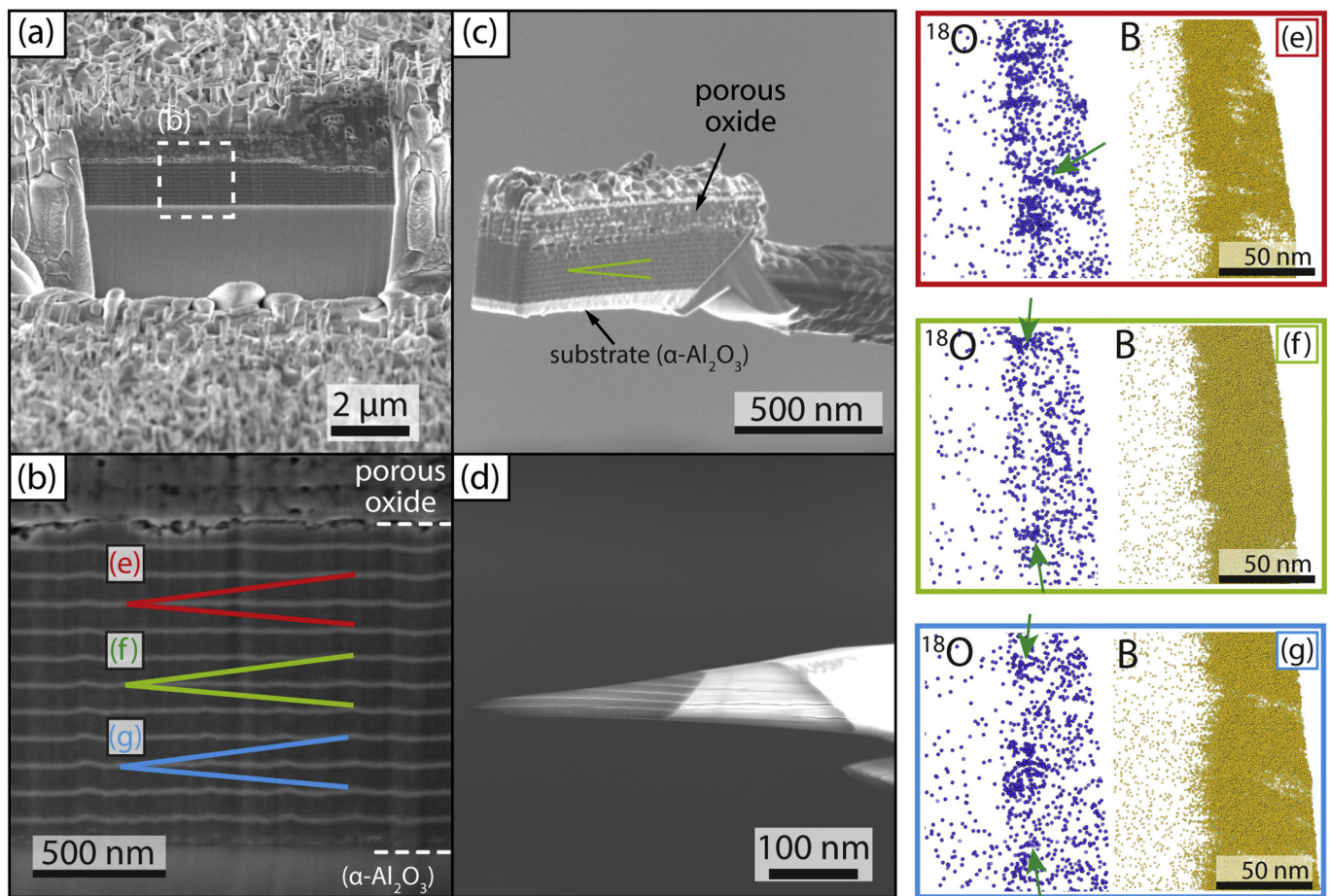


Fig. 3. APT analysis of tracer diffusion of ^{18}O in the layered system after subsequent oxidation at 900°C in pure ^{16}O and ^{18}O for 30 and 60 min, respectively. From the oxidized coating (a), three APT samples were extracted at various distances to the surfaces (b). Afterwards, they were lifted out and attached to a support structure (c) and subsequently prepared for the APT measurement (d). The elemental distribution of ^{18}O (blue) and B (yellow) for the surface near region (closest to the visual scale), the middle of the coating and towards the substrate is presented in (e), (f), and (g).

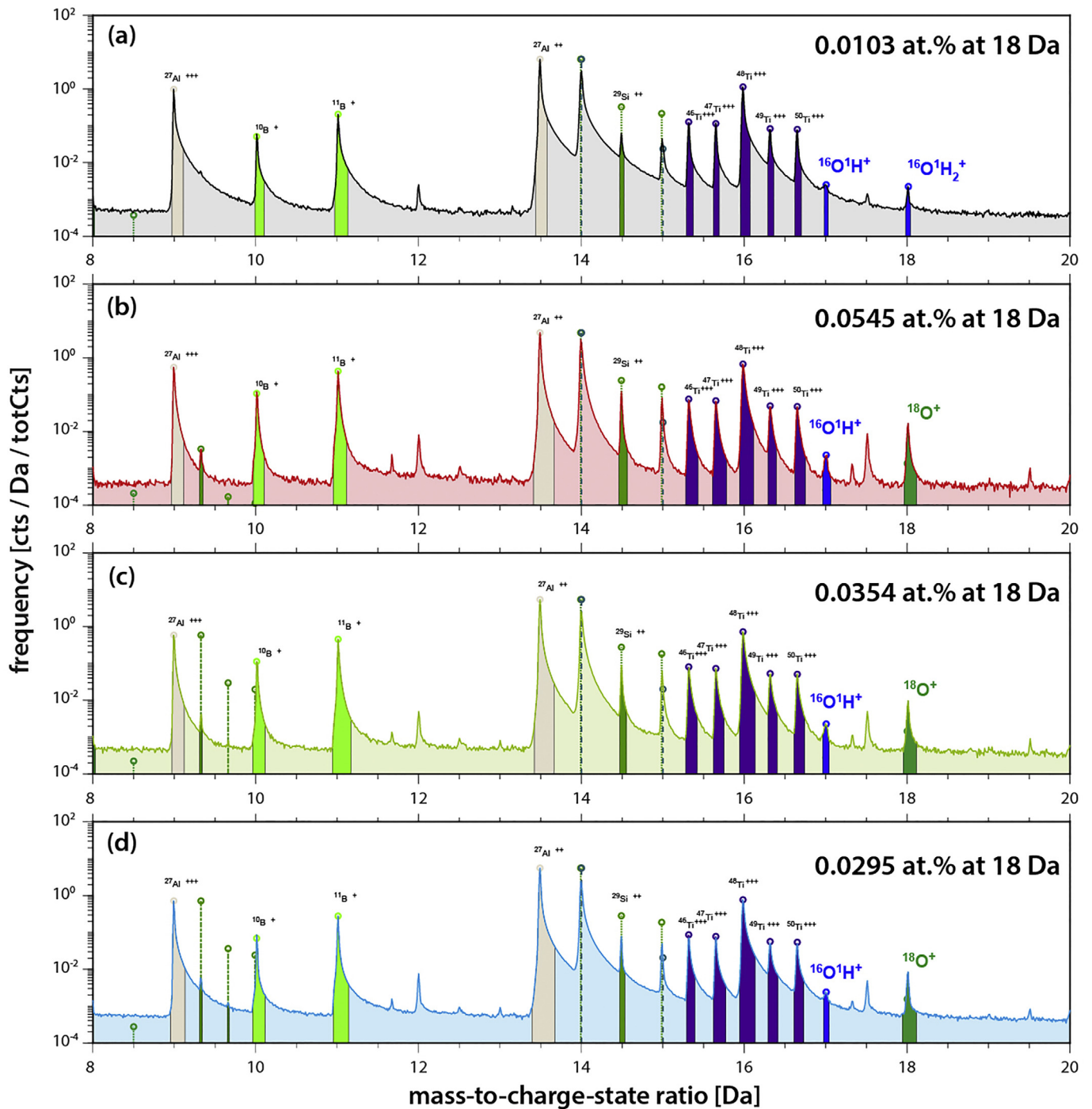


Fig. 4. Cut out between 8 to 20 Da of the mass to charge-state ratio of the APT tip of the as deposited coating (a) having $\Lambda = 130$ nm (presented in Fig. 1 and 2), and the corresponding oxidized APT tips – see also Fig. 3e to g – in (b) to (d), respectively. To clarify the increasing amount of $^{18}\text{O}^+$ compared to $^{16}\text{OH}_2^+$, the ranged peaks are highlighted in blue and green. After oxidizing the samples in ^{18}O at 900 °C for 60 min (30 min peroxidation in ^{16}O), a clear increase at 18 Da is recognizable.

is significantly higher within the Mo-Si-B layers than within the Ti-Al-N layers, see Fig. 3e-g. This suggests a very fast oxygen inward diffusion through Ti-Al-N layers and simultaneously for a high oxygen affinity of the Mo-Si-B layers.

Furthermore, a quantitative analysis of the data sets indicates a decreasing oxygen content from the oxide scale near region to the substrate/coating interface near specimen. Considering the surprisingly high permeability of Ti-Al-N for ^{18}O , the retarding effect of Mo-Si-B on the oxygen diffusion is evident. However, a more detailed investigation on the clustering behavior of ^{18}O within the Mo-Si-B layers shows

oxygen free areas besides a pathway network (Fig. 5a and b). This suggests a preferential oxygen diffusion along triple junctions (indicated by green arrows in Fig. 3e to g) between precipitated phases – most likely thermally driven. As shown in our previous study of thermally treated and oxidized Ti-Al-N/Mo-Si-B coatings using

spatially resolved nanobeam X-ray diffraction in transmission geometry [51], the intact coating material underneath the formed oxide scale does not show any formed oxides, but an evolution of intermetallic $\text{T}_1\text{-Mo}_5\text{Si}_3$ and $\text{T}_2\text{-Mo}_5\text{SiB}_2$ based phases. The crystallization of the as-deposited amorphous Mo-Si-B is furthermore accompanied by the

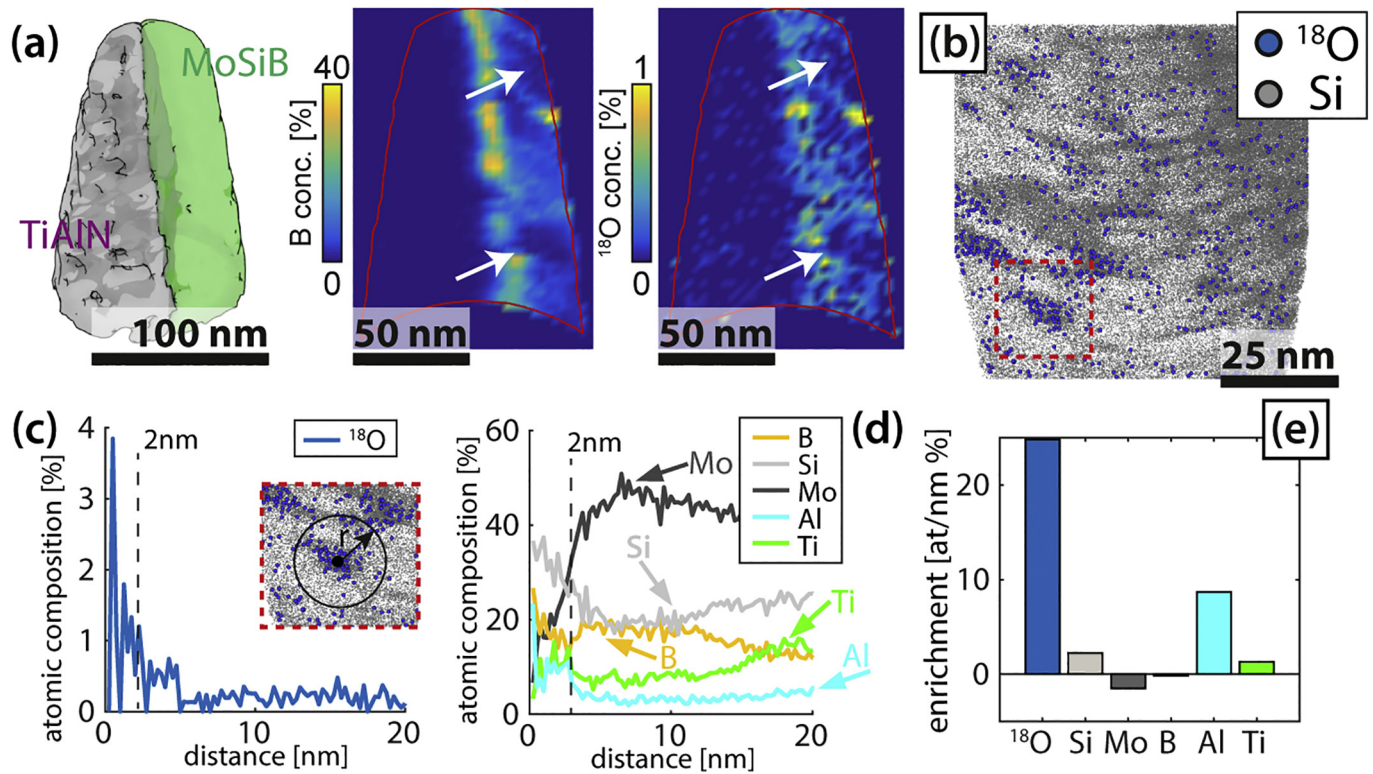


Fig. 5. Quantitative analysis of the tip extracted out of the oxide scale near region after subsequent oxidation at 900 °C in ^{16}O and ^{18}O for 30 and 60 min, respectively. The B and ^{18}O concentrations are presented in (a) and the ^{18}O and Si in (b). The chemical environment of an ^{18}O cluster (as marked in (b)) was analyzed by constructing a spherical volume element. The corresponding elemental profiles are given in (c) for ^{18}O and (d) for B, Si, Mo, Al, and Ti. By comparing the elemental composition within the 2 nm range with the average composition in the region of interest, we calculated the enrichment of the cluster with ^{18}O , Si, Mo, B, Al, and Ti (e).

decomposition of fcc Ti-Al-N into TiN and hexagonal, wurtzite structured AlN [52]. Consequently, the thermal load on the coating material leads to a crystallization of the initially amorphous Mo-Si-B interlayers, but no pronounced oxide formation. The resulting grain boundary phase between the precipitated grains generates a continuous network of triple junctions, which functions as a diffusion pathway for the incoming oxygen species.

In order to analyze the movement of ^{18}O through the Mo-Si-B layer during oxidation, we performed detailed clustering analyses of the specimen extracted from the region directly underneath the oxide scale. In Fig. 5a, the B and ^{18}O concentrations are compared. In both figurative representations, B and ^{18}O depleted sites share the same areas, associable with precipitated $\text{T}_1\text{-Mo}_5\text{Si}_3$ grains. Simultaneously, the probed volume also exhibits areas with significantly higher B content, possibly representing $\text{T}_2\text{-Mo}_5\text{SiB}_2$ crystallites. In between, the ^{18}O distribution forms a dense network with high concentrations next to small ^{18}O depleted areas. This suggests for a diffusion of ^{18}O between these precipitates. In Fig. 5b, the elemental distributions of Si and

^{18}O are presented, as viewed from a different perspective (about 45° rotated to the MoSiB layer as depicted in Fig. 5a – green schematic). Here, strong clustering of Si atoms is evident, indicating again the precipitation of $\text{T}_1\text{-Mo}_5\text{Si}_3$ and $\text{T}_2\text{-Mo}_5\text{SiB}_2$ based phases. The areas with very high Si concentrations are mostly free of ^{18}O , which preferably occupies sites in between. This proves ^{18}O diffusion along formed grain boundaries between the crystallized T_1 and T_2 phases. For a quantitative evaluation of the ^{18}O enriched clusters between the crystalline phases, we exclusively looked at the area as marked in Fig. 5b and c and calculated a radial concentration profile with its center in the middle of the cluster. The ^{18}O content is highest in the cluster center (~4 at%) and rapidly decreases to ~0.1 % after 2 nm, see Fig. 5c. In Fig. 5d, the atomic contents of B, Si, Mo, and Al are shown, calculated for the same volume

element as in Fig. 5c. The profile of Al and Si follow the trend of ^{18}O , also showing a maximum in the center of ~20 and 38 at%, respectively. After ~2 nm, the contents of Al (~7 at%) and Si (~20 at%) decrease significantly. The contents of B and Ti are almost constant at ~19 and ~10 at%, respectively. In contrast, the Mo fraction is low at high ^{18}O containing sites and steeply increases after passing the 2 nm barrier.

Additionally, we determined the enrichment of the grain boundary phase with ^{18}O , B, Si, Mo, Al, and Ti. Therefore, we compared the average elemental concentration within the 2 nm range with the elemental concentration of the region of interest, see Fig. 5d. In summary, the data clearly indicates an increased concentration of ^{18}O and Al along formed grain boundaries as well as a small enrichment of Ti and Si within the phases arising. Therefore, we expect that Al, originating from the cross-deposition during the synthesis process (or also from diffusing Al after the spinodal decomposition of the Ti-Al-N), do not form a solid solution with the Mo-rich intermetallic phases and, therefore, is preferably populating the grain boundary phase. Also, the uniform distribution of Ti within the analyzed volume suggests for the formation of a $\text{T}_1\text{-(Mo,Ti)}_5\text{Si}_3$ and $\text{T}_2\text{-(Mo,Ti)}_5\text{SiB}_2$ solid solutions, since Ti is known as a phase stabilizer for the T_1 and T_2 phase [53].

3.3. Improved coating design

These results allow to derive very specific strategies in order to improve the oxidation resistance and mechanical properties of the Ti-Al-N/Mo-Si-B multilayer system. As we found during the APT investigations, the oxygen migrates preferably along triple junctions between T_1 and T_2 precipitates within the Mo-Si-B layers. Consequently, controlling the crystal structure as well as the phase composition and morphology in the as-deposited state and upon thermal load potentially mitigates the oxygen mobility.

Our recent investigations on homogeneously grown magnetron sputtered $\text{Mo}_{1-x}\text{Ti}_x\text{Si}_{0.30}\text{B}_{0.20}$ thin films with $x = 0.05$ and 0.10 at% Ti showed the best oxidation resistance when applying a bias potential of -20 V and using the $\text{Mo}_{0.50}\text{Si}_{0.30}\text{B}_{0.20}$ target composition (while keeping the other parameters as described in this manuscript). This setup leads to an as-deposited amorphous state and also to the formation of the T_1 and T_2 phase upon vacuum annealing. However, we also found that, with an increasing bias potential, the crystalline character of these Mo-Si-B layers increases, apparently reducing the oxidation resistance. Additionally, we could resume that oxygen shows a strong association to Al when migrating through the Mo-Si-B layers, originating from the specific process design. An explanation for this behavior can be given by thermodynamics, as Al has one of the lowest Gibbs free energy for the formation of oxide based compounds [54]. Since the process stability requires to run all targets permanently – a continuous re-igniting of the arc evaporated Ti-Al cathodes potentially cause process instabilities – the multilayer arrangement was realized by covering the respective targets with shutters. However, a significant reduction of the cathode current potentially reduces the cross-deposition of Al and Ti within the Mo-Si-B layers.

Based on all these findings, the architectural design was adapted according to our previous studies [33,35,38], so that the Mo-Si-B layers are as thin as possible while a complete interruption of the re-nucleating Ti-Al-N laminates is still assured. This guarantees excellent mechanical properties in combination with an effective interruption of continuous grain boundaries, ranging from the coating/substrate interface to the surface. Therefore, we deposited an improved multilayer with an optimized bilayer period of $\Lambda \sim 32$ nm with $\lambda_{\text{Ti-Al-N}} \sim 26$ nm and $\lambda_{\text{Mo-Si-B}} \sim 6$ nm and a total number of 80 bilayers. An inverted high angle annular dark field (HAADF) micrograph of the optimized multilayer is displayed in Fig. 6a. Here, a 111 diffraction spot was exclusively surveyed with the selected area electron diffraction (SAED) aperture in order to highlight the growth mode of the Ti-Al-N grains. The image clearly suggests an

effective interruption of the Ti-Al-N grains and a consistent limitation of the grain size to the Ti-Al-N layer thickness, assuring the functionality of the proposed multilayer design. The respective HR-TEM image, Fig. 6b, again shows the 26 nm thin Ti-Al-N layers and 6 nm thin Mo-Si-B layers. The micrograph clearly indicates the re-nucleation of the Ti-Al-N grain as well as their intermittent growth mode, exemplary highlighted by the dashed line for a single Ti-Al-N grain, see Fig. 6b. Additionally, we investigated the crystal structure by means of FFT (not shown in the graph), finding the Ti-Al-N to be single phased fcc as well as the Mo-Si-B to be amorphous.

A detailed 3D chemical analysis of the Ti-Al-N and the Mo-Si-B layer with respect to the cross-contamination of the optimized multilayer system was done by means of APT. The reconstructed APT specimen, focusing on the distribution of B as well as 2D elemental maps of Al, Ti, and B (representing the same region of interest) is shown in Fig. 6c. The data set indicates very sharp interfaces as well as a constant bilayer period across the whole length of the tip.

Furthermore, we calculated a line scan across two bilayers, only considering B and Ti in order to avoid peak overlaps (e.g. Si and N at 14 D and 28 Dalton as well as BO^+ and Al at 27 D), see Fig. 6d. Consequently, only the relative elemental composition is shown. Even though there are still contaminations visible in the Mo-Si-B layer, the cross-contamination could be clearly reduced (compare Fig. 2 and ref. [33]). The highly concentrated B in the Mo-Si-B layer shows almost no cross-deposition in the Ti-Al-N layer, being again representative for very sharp interfaces.

3.4. Oxidation resistance and kinetics

In order to prove the effectiveness of the derived strategies, we investigated the oxidation performance using thermo-gravimetry in an oxidative environment (all on free-standing coating material). Therefore, we compared the multilayer initially investigated in this study

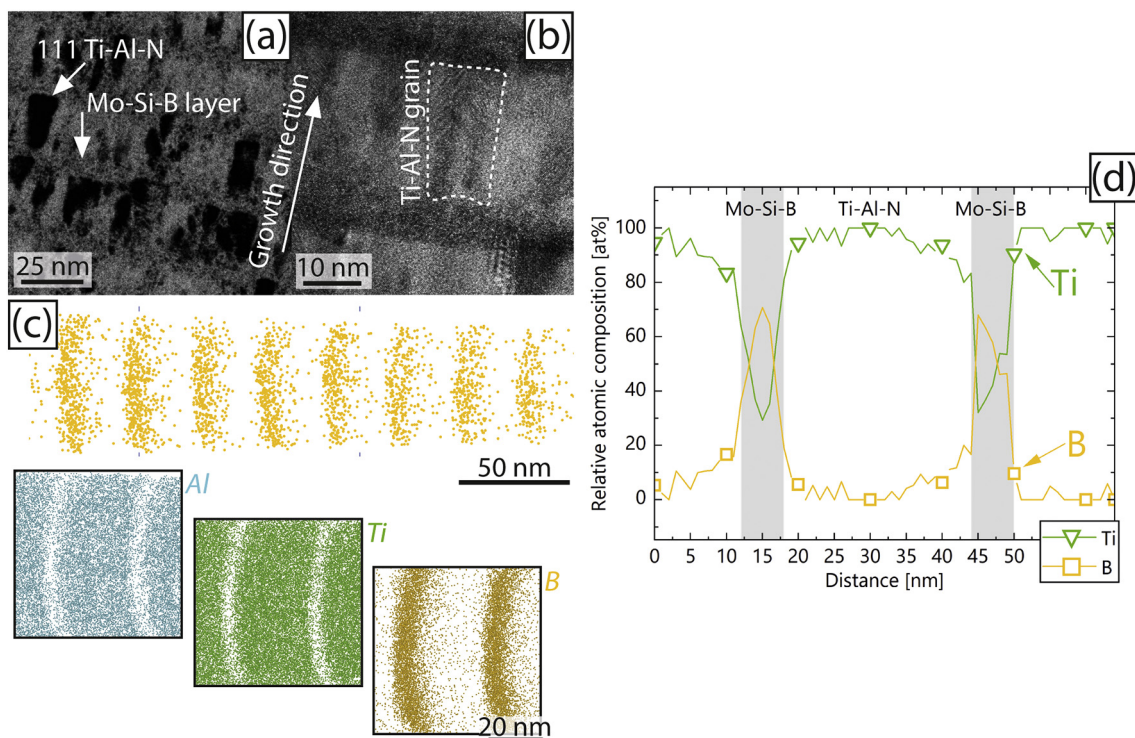


Fig. 6. Inverted HAADF micrograph (a) and HR-TEM image (b) as well as detailed APT investigations (c) of the optimized multilayer system ($\Lambda = 32$ nm) in the as-deposited state, highlighting the total interruption of continuous column boundaries, ranging from the substrate/coating interface to the surface and showing only minor cross-deposition of Ti and Al within the Mo-Si-B layer. (d) Shows an EDX line scan across two bilayers by displaying the relative atomic composition of B and Ti, showing the reduced cross-contamination during deposition.

($\Lambda = 130$ nm) as well as the coating as described in our previous studies [33,35,38] ($\Lambda = 37$ nm with $\lambda_{\text{Ti-Al-N}} = 31$ nm and $\lambda_{\text{Mo-Si-B}} = 6$ nm, synthesized with -65 V bias and no reduced cathode current during the Mo-Si-B synthesis) with the abovementioned optimized version ($\Lambda = 32$ nm, -20 V bias potential and a reduced cathode current of 50 A during the Mo-Si-B synthesis). The thermo-gravimetric mass change curves after isothermal oxidation at 800 , 900 and 1000 °C for 7 h are shown in Figs. 6a-c, respectively.

After oxidation at 800 °C, Fig. 7a, the multilayer with a bilayer period of $\Lambda = 130$ nm shows a rapid mass gain of $\sim 20\%$, followed by a significant and steady mass loss. A decrease in mass in this temperature range can be assigned to the formation of volatile MoO_x species, as this mechanism was described in detail for Mo-Si-B based alloys [52] and in our previous work based on detailed XRD studies of an oxidized Ti-Al-N/Mo-Si-B multilayer system [38]. For the other investigated coatings ($\Lambda = 37$ nm and $\Lambda = 32$ nm), the curves are also characterized by an initial mass gain, but following a parabolic behavior (obtaining a linear and a subsequent parabolic part), being characteristic for stable scales. However, the mass gain in this parabolic regime is more pronounced for the optimized multilayer ($\Lambda = 32$ nm) – plus 10% mass gain compared to 5% for the one with $\Lambda = 37$ nm. Nevertheless, the steady profile indicates a strong influence of the bilayer period and is representative for a stable oxidation performance, following a parabolic rate law.

At 900 °C, Fig. 7b, the multilayered coating with a bilayer period of $\Lambda = 130$ nm oxidizes immediately after introducing synthetic air and subsequently experiences a rapid mass loss. The pronounced spike in the mass gain curve for this bilayer period is possibly related to a rapid evaporation of the relatively thick Mo-Si-B layers, before the formation of a dense oxide scale can occur. Here, also the kinetic difference between free-standing coating materials and films on hard substrates in oxidative environments is evident, as this coating formed an adherent scale in the combined ^{18}O and ^{16}O heat treatments used for the APT investigations after overall 90 min at 900 °C – see Fig. 3a. The two optimized versions – multilayers with $\Lambda = 37$ nm and $\Lambda = 32$ nm, respectively – exhibit a very similar parabolic behavior at 900 °C. Here, no significant differences in mass gains were detectable between the two versions.

At 1000 °C, Fig. 7c, the situation changes drastically. The $\Lambda = 130$ nm multilayer oxidizes immediately, also showing a pronounced spike, comparable to 900 °C, whereas the $\Lambda = 37$ nm multilayer shows a peak in mass gain after 3 h followed by a pronounced decrease, being indicative for a volatile removal of the formed oxide. Hence, the coating obtaining inhomogeneities within the amorphous Mo-Si-B diffusion barrier fails, as short circuit diffusion along the abovementioned Al decorated triple junctions is predominant. In contrast, the perfectly shaped

multilayer system ($\Lambda = 32$ nm) still established a dense adherent scale, exhibiting a parabolic oxide growth mode with an overall mass gain of only $\sim 8\%$.

The oxidation performance was additionally investigated by oxidizing the discussed multilayer systems, applying the identical environmental conditions as for the thermo-gravimetric analysis. In Fig. 8a, the $\Lambda = 130$ nm multilayer is shown after annealing at 900 °C for 1.5 h. If compare this to the $\Lambda = 37$ nm multilayer, also oxidized at 900 °C but for 7 h, a clear enhancement due to the changed architecture is obvious. However, as we also intended to optimize the Ti-Al-N/Mo-Si-B multilayer regarding the deposition parameters and the chemical integrity, we also oxidized the $\Lambda = 37$ nm and $\Lambda = 32$ nm multilayer coating at 1100 °C for 7 h, see Fig. 8b_{II} and c, respectively. While the $\Lambda = 37$ nm coating is already fully oxidized after this harsh treatment, the $\Lambda = 32$ nm multilayer still shows 4.3 μm remaining coating thickness (out of 6.0), proving the efficiency of the undertaken measures – especially, applying amorphous diffusion barriers to decelerate oxygen inward diffusion along preferred diffusion pathways. These results also nicely confirm the assessment based on the presented thermo-gravimetric investigations.

In order to quantify the oxidation kinetics, we also calculated the oxidation rate constants for the obtained mass evolution according to references [24, 55]. As the oxide formation either follows a linear or parabolic rate law, the thermo-gravimetric curves were divided into Regime 1 (linear behavior, $k_{\text{linear}} (k_l)$) and Regime 2 (parabolic behavior, $k_{\text{parabolic}}^* (k_p^*)$). For the coating having a bilayer period of $\Lambda = 130$ nm, we observed an exclusively linear behavior, followed by a significant mass loss for all oxidation temperatures (see Fig. 7a-c). Hence, this bilayer period exhibits the highest k_l values of around $5 \cdot 10^{-3} \text{ s}^{-1}$ between 800 and 1000 °C.

The multilayers having a bilayer period of $\Lambda = 37$ nm and $\Lambda = 32$ nm reveal both a parabolic character, therefore k_l and k_p^* according to Regime 1 and 2 were estimated, respectively. The full data set of the oxidation rate constants is given in Table 1. In general, the oxidation kinetics of both coatings seems to be similar, but the coating with $\Lambda = 32$ nm (without any inhomogeneities within the amorphous diffusion barriers) exhibits by far the lowest linear rate constants (e.g. k_l value of $8.9 \cdot 10^{-5} \text{ s}^{-1}$ at 900 °C). Consequently, the oxide growth mode changes instantly to parabolic behavior leading to the formation of dense and adherent scales. In comparison to previous oxidation studies, e.g. monolithic (Ti,Al,Ta)N obtaining a value of $2.40 \cdot 10^{-4} \text{ s}^{-1}$ at 950 °C, the kinetics seems to be clearly retarded [24]. Furthermore, other studies showed that monolithic Ti-Al-N and alloyed Ti-Al-X-N failed latest after 5 h at 950 °C [56].

Previous studies on Mo-Si-B based alloys as bulk material suggest for an excellent oxidation resistance in the high temperature range. However, at lower temperatures (< 900 – 1000 °C), the material is prone to

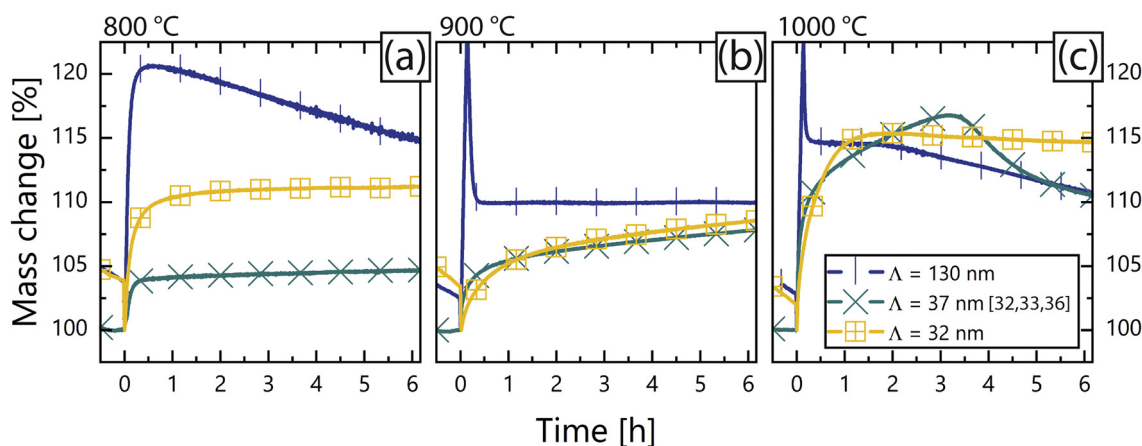


Fig. 7. Thermo-gravimetric mass-change curves during isothermally oxidation in synthetic air at (a) 800 , (b) 900 , and (c) 1000 °C of $\Lambda = 130$ nm (blue lines with strokes), $\Lambda = 37$ nm (cyan lines with crosses), and $\Lambda = 32$ nm (yellow lines with squares) multilayer coatings, respectively.

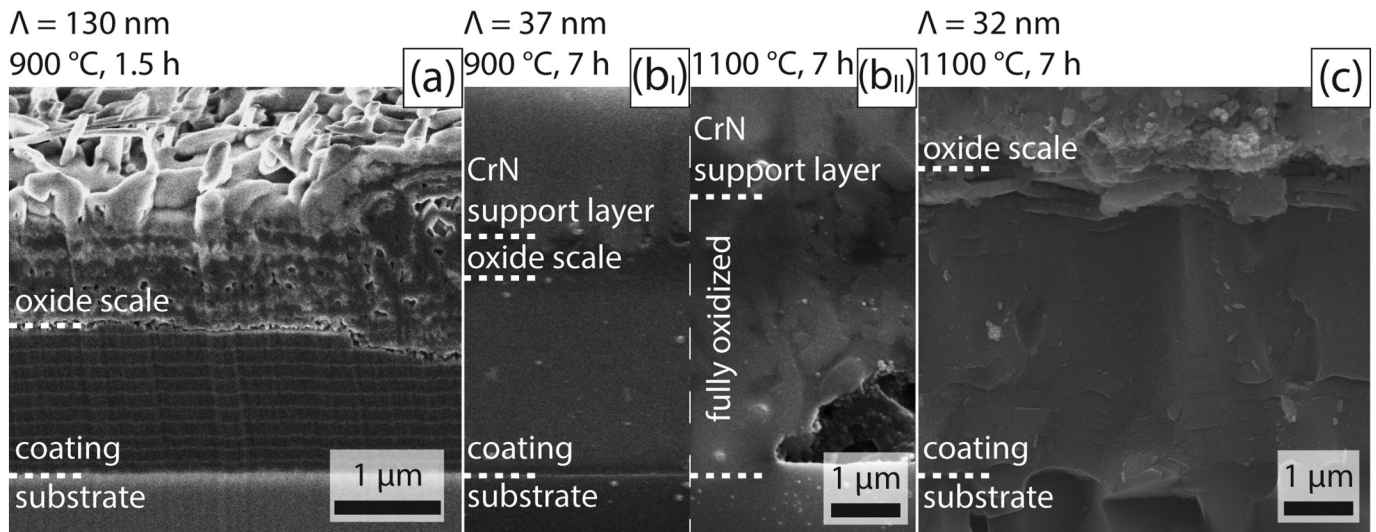


Fig. 8. Cross-sectional SEM micrographs of the investigated multilayers after oxidation on Al_2O_3 substrate materials. (a) and (b) showing the $\Lambda = 130$ nm (1.5 h) and $\Lambda = 37$ nm multilayer (7 h), respectively. The $\Lambda = 37$ nm and $\Lambda = 32$ nm multilayer oxidized at 1100 °C for 7 h are shown in (b_i) and (c), respectively.

Table 1

Rate constants k_l , k_p^* obtained from the DSC mass change curves for 800, 900, and 1100 °C.

Coating #	$k_{\text{linear}}(m = k_l \cdot t), k_{\text{parabolic}}\left(\left(\frac{\Delta m}{m_0}\right)^2 = k_p^* \cdot t\right); [1/s]$					
	800 °C		900 °C		1000 °C	
	k_l	k_p^*	k_l	k_p^*	k_l	k_p^*
$\Lambda = 130$ nm	$3.3 \cdot 10^{-3}$	-*	$6.5 \cdot 10^{-3}$	-*	$5.6 \cdot 10^{-3}$	-*
$\Lambda = 37$ nm	$9.2 \cdot 10^{-4}$	$2.5 \cdot 10^{-8}$	$7.4 \cdot 10^{-4}$	$1.6 \cdot 10^{-7}$	$9.8 \cdot 10^{-4}$	-*
$\Lambda = 32$ nm	$1.3 \cdot 10^{-4}$	$4.4 \cdot 10^{-8}$	$8.9 \cdot 10^{-5}$	$1.9 \cdot 10^{-7}$	$4.7 \cdot 10^{-4}$	-*

* After an initial linear mass gain, these coating show a significant mass loss and therefore do not allow for a determination of the parabolic rate constant k_p^* .

the formation of volatile MoO_x and B_2O_3 surface evaporation before a stable oxidation state can be reached [57]. For the $\Lambda = 130$ nm coating at 900 and 1000 °C, the thickness of the Mo-Si-B layer (being 30 nm) does not allow for the formation of a dense and stable scale, as it can be seen in Fig. 3a. However, for smaller bilayer periods, the thin Mo-Si-B layer and its retarding effect on the oxygen inward diffusion into the Ti-Al-N layer allow for the formation of a dense scale, leading to a significantly improved oxidation resistance and lower oxidation rate constants.

4. Conclusion

Our work proves a significant oxygen diffusion ahead of a visually and chemically recognizable oxide scale within investigated Ti-Al-N/Mo-Si-B multilayers. Moreover, within these highly crystalline Ti-Al-N layers, nearly no ^{18}O species could be found, emphasizing grain boundary diffusion being decisive over bulk diffusion (within the prevalent columnar grains) for oxidation processes. We could also show the strong tendency of Mo-Si-B to form oxygen enriched areas, representing a sponge-like behavior within these nanostructured layers, consequently slowing down the oxygen inward diffusion. Based on these findings, we derived a concept based on minimized oxygen mobility during high-temperature oxidation. The resulting multilayer yields a stable oxidation state up to 1100 °C for 7 h, obtaining a remaining coating thickness of 4.3 μm out of 6.0 μm in the as-deposited state. In comparison, monolithic Ti-Al-N as well as alloyed Ti-Al-X-N coatings fail latest at 950 °C after 5 h. The detailed investigations on diffusion pathways during high temperature oxidation emphasize the importance of fast diffusion

pathways such as grain and column boundaries in addition to the chemistry. Hence, the morphology and architecture of coating materials is decisive for oxidation kinetics.

Data availability

The data that support the findings of this study are available from the corresponding author upon reasonable request.

Declaration of Competing Interest

The authors declare that they have no known competing financial interests or personal relationships that could have appeared to influence the work reported in this paper.

Acknowledgement

The financial support by the Austrian Federal Ministry for Digital and Economic Affairs and the National Foundation for Research, Technology and Development is gratefully acknowledged (Christian Doppler Laboratory "Surface Engineering of high-performance Components"). We also thank for the financial support of Plansee SE, Plansee Composite Materials GmbH, and Oerlikon Balzers, Oerlikon Surface Solutions AG. Part of this project has received funding from the European Research Council (ERC) under the European Union's Horizon 2020 research and innovation program under grant agreement No 805065. In addition, we want to thank the X-ray center (XRC) of TU Wien for beam time as well as the electron microscopy center - USTEM TU Wien - for using the SEM and TEM facilities.

References

- [1] G. Gottstein, *Physikalische Grundlagen der Materialkunde*, Springer, Berlin Heidelberg, Berlin, Heidelberg, 2007.
- [2] A. Fick, Ueber Diffusion, *Ann. Der Phys. Und Chemie*. 170 (1855) 59–86, <https://doi.org/10.1002/andp.18551700105>.
- [3] G.D. Preston, Structure of Age-Hardened Aluminium-Copper Alloys, *Nature*. 142 (1938) 570, <https://doi.org/10.1038/142570a0>.
- [4] W.D. Kingery, Densification during Sintering in the Presence of a Liquid Phase, I. Theory, *J. Appl. Phys* 30 (1959) 301–306, <https://doi.org/10.1063/1.1735155>.
- [5] J.W. Cahn, On spinodal decomposition, *Acta Metall.*, <http://www.scopus.com/citation/output.url?origin=recordpage&view=&src=s&eid=2-s2.0-43449102981&outputType=export> 1961. (Accessed 6 April 2012).
- [6] C.V. Ramana, S. Utsunomiya, R.C. Ewing, U. Becker, V.V. Atuchin, V.S. Aliev, et al., Spectroscopic ellipsometry characterization of the optical properties and thermal

- stability of ZrO₂ films made by ion-beam assisted deposition, *Appl. Phys. Lett.* 92 (2008), 011917, <https://doi.org/10.1063/1.2811955>.
- [7] G. Tammann, Über Anlauffarben von Metallen, *Zeitschrift Für Anorg. Und Allg. Chemie.* 111 (1920) 78–89, <https://doi.org/10.1002/zaac.19201110107>.
- [8] N. Pilling, R.J. Bedworth, The Oxidation of Metals at High Temperatures, *Inst. Met.* 29 (1923) 529.
- [9] G.H. Meier, F.S. Pettit, N. Birks, Interactive mechanisms in the high-temperature oxidation of metals, in: *High-Temperature Oxid.*, Elsevier, Sulphidation Process., 1990 1–15, <https://doi.org/10.1016/B978-0-08-040423-3.50005-7>.
- [10] P.H. Mayrhofer, R. Rachbauer, D. Holec, F. Rovere, J.M. Schneider, Protective Transition Metal Nitride Coatings, in: *Compr. Elsevier, Mater. Process.*, 2014 355–388, <https://doi.org/10.1016/B978-0-08-096532-1.00423-4>.
- [11] A. Atkinson, Transport processes during the growth of oxide films at elevated temperature, *Rev. Mod. Phys.* 57 (1985) 437–470, <https://doi.org/10.1103/RevModPhys.57.437>.
- [12] A. Atkinson, R.I. Taylor, The diffusion of Ni in the bulk and along dislocations in NiO single crystals, *Philos. Mag.* A. 39 (1979) 581–595, <https://doi.org/10.1080/01418617908239293>.
- [13] G. Ben Abderrazik, Growth mechanism of Al₂O₃ scales developed on Fe Cr Al alloys, *Solid State Ionics.* 22 (1987) 285–294, [https://doi.org/10.1016/0167-2738\(87\)90146-9](https://doi.org/10.1016/0167-2738(87)90146-9).
- [14] S. Piazzolo, A. La Fontaine, P. Trimby, S. Harley, L. Yang, R. Armstrong, et al., Deformation-induced trace element redistribution in zircon revealed using atom probe tomography, *Nat. Commun.* 7 (2016) 1–7, <https://doi.org/10.1038/ncomms10490>.
- [15] M. Vaidya, K.G. Pradeep, B.S. Murty, G. Wilde, S.V. Divinski, Radioactive isotopes reveal a non sluggish kinetics of grain boundary diffusion in high entropy alloys, *Sci. Rep.* 7 (2017) 12293, <https://doi.org/10.1038/s41598-017-12551-9>.
- [16] J.T. Cukjati, R.F. Cooper, S.W. Parman, N. Zhao, A.J. Akey, F.A.T.P. Laiginhas, Differences in chemical thickness of grain and phase boundaries: an atom probe tomography study of experimentally deformed wehrlite, *Phys. Chem. Miner.* 46 (2019) 845–859, <https://doi.org/10.1007/s00269-019-01045-x>.
- [17] K. Schweinar, R.L. Nicholls, R.R. Rajamathi, P. Zeller, M. Amati, L. Gregoratti, et al., Probing catalytic surfaces by correlative scanning photoemission electron microscopy and atom probe tomography, *J. Mater. Chem. A* 8 (2020) 388–400, <https://doi.org/10.1039/c9ta10818a>.
- [18] O. Madelung, U. Rössler, M. Schulz, Chromium sesquioxide (Cr₂O₃): thermal expansion, density, melting point, Non-Tetrahedrally Bond. Bin. Compd. II, Springer-Verlag, Berlin/Heidelberg 2020, pp. 1–2, https://doi.org/10.1007/10681735_651.
- [19] N. Ishizawa, T. Miyata, I. Minato, F. Marumo, S. Iwai, A structural investigation of α-Al₂O₃ at 2170 K, *Acta Crystallogr. Sect. B Struct. Crystallogr. Cryst. Chem.* 36 (1980) 228–230, <https://doi.org/10.1107/S0567740880002981>.
- [20] D. Caplan, G.I. Sproule, Effect of oxide grain structure on the high-temperature oxidation of Cr, *Oxid. Met.* 9 (1975) 459–472, <https://doi.org/10.1007/BF00611694>.
- [21] F. Vaz, L. Rebouta, M. Andritschky, M.F. da Silva, J.C. Soares, Thermal oxidation of Ti_{1-x}Al_xN coatings in air, *J. Eur. Ceram. Soc.* 17 (1997) 1971–1977, [https://doi.org/10.1016/S0955-2219\(97\)00050-2](https://doi.org/10.1016/S0955-2219(97)00050-2).
- [22] L. Chen, J. Paulitsch, Y. Du, P.H. Mayrhofer, Thermal stability and oxidation resistance of Ti–Al–N coatings, *Surf. Coatings Technol.* 206 (2012) 2954–2960, <https://doi.org/10.1016/j.surfcoat.2011.12.028>.
- [23] G. Greczynski, L. Hultman, M. Odén, X-ray photoelectron spectroscopy studies of Ti_{1-x}Al_xN (0 ≤ x ≤ 0.83) high-temperature oxidation: The crucial role of Al concentration, *Surf. Coatings Technol.* 374 (2019) 923–934, <https://doi.org/10.1016/j.surfcoat.2019.06.081>.
- [24] R. Hollerweger, H. Riedl, J. Paulitsch, M. Arndt, R. Rachbauer, P. Polcik, et al., Origin of high temperature oxidation resistance of Ti–Al–Ta–N coatings, *Surf. Coatings Technol.* 257 (2014) <https://doi.org/10.1016/j.surfcoat.2014.02.067>.
- [25] F. Seitz, On the porosity observed in the Kirkendall effect, *Acta Metall.* 1 (1953) 355–369, [https://doi.org/10.1016/0001-6160\(53\)90112-6](https://doi.org/10.1016/0001-6160(53)90112-6).
- [26] F.H. Stott, The Oxidation of Alumina-Forming Alloys, *Mater. Sci. Forum.* 251–254 (1997) 19–32, <https://doi.org/10.4028/www.scientific.net/MSF.251-254.19>.
- [27] F.H. Stott, G.C. Wood, Growth and adhesion of oxide scales on Al₂O₃-forming alloys and coatings, *Mater. Sci. Eng.* 87 (1987) 267–274, [https://doi.org/10.1016/0025-5416\(87\)90388-0](https://doi.org/10.1016/0025-5416(87)90388-0).
- [28] T. Li, O. Kasian, S. Cherevko, S. Zhang, S. Geiger, C. Scheu, et al., Atomic-scale insights into surface species of electrocatalysts in three dimensions, *Nat. Catal.* 1 (2018) 300–305, <https://doi.org/10.1038/s41929-018-0043-3>.
- [29] I. Petrov, P.B. Barna, L. Hultman, J.E. Greene, Microstructural evolution during film growth, *J. Vac. Sci. Technol. A Vacuum, Surfaces, Film* 21 (2003) 117–S128, <https://doi.org/10.1116/1.1601610>.
- [30] M.-H. Tsai, C.-W. Wang, C.-H. Lai, J.-W. Yeh, J.-Y. Gan, Thermally stable amorphous (Al_{1-x}Nb_xSiTaTiVZr)₅₀N₅₀ nitride film as diffusion barrier in copper metallization, *Appl. Phys. Lett.* 92 (2008), 052109, <https://doi.org/10.1063/1.2841810>.
- [31] M. Stueber, H. Holleck, H. Leiste, K. Seemann, S. Ulrich, C. Ziebert, Concepts for the design of advanced nanoscale PVD multilayer protective thin films, *J. Alloys Compd.* 483 (2009) 321–333, <https://doi.org/10.1016/j.jallcom.2008.08.133>.
- [32] M. Stueber, C. Ziebert, H. Leiste, S. Ulrich, C. Sanz, E. Fuentes, et al., WEAR STUDIES AND CUTTING TESTS OF Ti – Al – N – C NANOCOMPOSITE COATINGS IN MILLING OPERATIONS – TECHNICAL COMMUNICATION, *Mach. Sci. Technol.* 13 (2009) 122–141, <https://doi.org/10.1080/10910340902782687>.
- [33] E. Aschauer, S. Sackl, T. Schachinger, T. Wojcik, H. Bolvardi, M. Arndt, et al., Nanostructural investigation of Ti–Al–N/Mo–Si–B multilayer coatings: A comparative study by APT and HR-TEM, *Vacuum.* 157 (2018) 173–179, <https://doi.org/10.1016/j.vacuum.2018.08.037>.
- [34] P.V. Kiryukhantsev-Korneev, I.V. Iatsyuk, N.V. Shvindina, E.A. Levashov, D.V. Shtansky, Comparative investigation of structure, mechanical properties, and oxidation resistance of Mo–Si–B and Mo–Al–Si–B coatings, *Corros. Sci.* 123 (2017) 319–327, <https://doi.org/10.1016/j.corsci.2017.04.023>.
- [35] H. Riedl, E. Aschauer, C.M. Koller, P. Polcik, M. Arndt, P.H. Mayrhofer, Ti–Al–N/Mo–Si–B multilayers: An architectural arrangement for high temperature oxidation resistant hard coatings, *Surf. Coatings Technol.* 328 (2017) <https://doi.org/10.1016/j.surfcoat.2017.08.032>.
- [36] H. Riedl, C.M. Koller, A. Limbeck, J. Kalaš, P. Polcik, P.H. Mayrhofer, Oxidation behavior and tribological properties of multilayered Ti–Al–N/Mo–Si–B thin films, *J. Vac. Sci. Technol. A Vacuum, Surfaces, Film* 33 (2015) 05E129, <https://doi.org/10.1116/1.4929536>.
- [37] H. Riedl, A. Vieweg, A. Limbeck, J. Kalaš, M. Arndt, P. Polcik, et al., Thermal stability and mechanical properties of boron enhanced Mo–Si coatings, *Surf. Coatings Technol.* 280 (2015) 282–290, <https://doi.org/10.1016/j.surfcoat.2015.09.015>.
- [38] E. Aschauer, S. Sackl, T. Schachinger, H. Bolvardi, M. Arndt, P. Polcik, et al., Atomic scale investigations of thermally treated nano-structured Ti–Al–N/Mo–Si–B multilayers, *Surf. Coatings Technol.* 349 (2018) 480–487, <https://doi.org/10.1016/j.surfcoat.2018.06.026>.
- [39] D.J. Tallman, B. Anasori, M.W. Barsoum, A Critical Review of the Oxidation of Ti 2 AlC, Ti 3 AlC 2 and Cr 2 AlC in Air, *Mater. Res. Lett.* 1 (2013) 115–125, <https://doi.org/10.1080/21663831.2013.806364>.
- [40] M. Gerstl, T. Frömling, A. Schintlmeister, H. Hutter, J. Fleig, Measurement of 180 tracer diffusion coefficients in thin yttria stabilized zirconia films, *Solid State Ionics.* 184 (2011) 23–26, <https://doi.org/10.1016/j.ssi.2010.08.013>.
- [41] G. Bakradze, L.P.H. Jeurgens, T. Acartürk, U. Starke, E.J. Mittemeijer, Atomic transport mechanisms in thin oxide films grown on zirconium by thermal oxidation, as-derived from 180-tracer experiments, *Acta Mater.* 59 (2011) 7498–7507, <https://doi.org/10.1016/j.actamat.2011.08.035>.
- [42] T.M. Huber, E. Navickas, K. Sasaki, B. Yildiz, H. Tuller, G. Friedbacher, et al., Experimental Design for Voltage Driven Tracer Incorporation and Diffusion Studies on Oxide Thin Film Electrodes, *J. Electrochem. Soc.* 164 (2017) F809–F814, <https://doi.org/10.1149/2.0711707jes>.
- [43] M.P. Brady, A.V. Levlev, M. Fayek, D.N. Leonard, M.G. Frith, H.M. Meyer, et al., Rapid Diffusion and Nanosegregation of Hydrogen in Magnesium Alloys from Exposure to Water, *ACS Appl. Mater. Interfaces.* 9 (2017) 38125–38134, <https://doi.org/10.1021/acsami.7b10750>.
- [44] M.K. Miller, K.F. Russell, Atom probe specimen preparation with a dual beam SEM/FIB miller, *Ultramicroscopy.* 107 (2007) 761–766, <https://doi.org/10.1016/j.ultramic.2007.02.023>.
- [45] J.E. Halpin, R.W.H. Webster, H. Gardner, M.P. Moody, P.A.J. Bagot, D.A. MacLaren, An in-situ approach for preparing atom probe tomography specimens by xenon plasma-focussed ion beam, *Ultramicroscopy.* 202 (2019) 121–127, <https://doi.org/10.1016/j.ultramic.2019.04.005>.
- [46] A. Huguet, A. Menand, Atom-probe determination of interstitial element concentration in two-phase and single-phase TiAl-based alloys, *Appl. Surf. Sci.* 76–77 (1994) 191–197, [https://doi.org/10.1016/0169-4332\(94\)90342-5](https://doi.org/10.1016/0169-4332(94)90342-5).
- [47] A. Anders, A structure zone diagram including plasma-based deposition and ion etching, *Thin Solid Films.* 518 (2010) 4087–4090, <https://doi.org/10.1016/j.tsf.2009.10.145>.
- [48] J.E. Daalder, Erosion and the origin of charged and neutral species in vacuum arcs erosion and the origin of charged and neutral species in vacuum arcs, *J. Appl. Phys.* 8 (1975) 1647.
- [49] C.M. Koller, J. Ramm, S. Kolozsvári, J. Paulitsch, P.H. Mayrhofer, Role of droplets and iron on the phase formation of arc evaporated Al–Cr-oxide coatings, *Surf. Coatings Technol.* 276 (2015) 735–742, <https://doi.org/10.1016/j.surfcoat.2015.05.012>.
- [50] D.L.J. Engberg, L.J.S. Johnson, J. Jensen, M. Thuvander, L. Hultman, Resolving mass spectral overlaps in atom probe tomography by isotopic substitutions – case of TiSi¹⁵N, *Ultramicroscopy.* 184 (2018) 51–60, <https://doi.org/10.1016/j.ultramic.2017.08.004>.
- [51] E. Aschauer, M. Bartosik, H. Bolvardi, M. Arndt, P. Polcik, A. Davydok, et al., Strain and stress analyses on thermally annealed Ti–Al–N/Mo–Si–B multilayer coatings by synchrotron X-ray diffraction, *Surf. Coatings Technol.* 361 (2019) 364–370, <https://doi.org/10.1016/j.surfcoat.2019.01.075>.
- [52] P.H. Mayrhofer, A. Hörling, L. Karlsson, J. Sjölen, T. Larsson, C. Mitterer, et al., Self-organized nanostructures in the Ti–Al–N system, *Appl. Phys. Lett.* 83 (2003) 2049–2051, <https://doi.org/10.1063/1.1608464>.
- [53] R. Sakidja, J.H. Perepezko, S. Kim, N. Sekido, Phase stability and structural defects in high-temperature Mo – Si – B alloys, *Acta Mater.* 56 (2008) 5223–5244, <https://doi.org/10.1016/j.actamat.2008.07.015>.
- [54] H.J.T. Ellingham, *Transactions and communications, J. Soc. Chem. Ind.* 63 (1944) 125–160, <https://doi.org/10.1002/jctb.5000524920>.
- [55] S. Mrowec, A. Stokosa, Calculations of parabolic rate constants for metal oxidation, *Oxid. Met.* 8 (1974) 379–391, <https://doi.org/10.1007/BF00603388>.
- [56] H. Asanuma, F.F. Klimashin, P. Polcik, S. Kolozsvári, H. Riedl, P.H. Mayrhofer, Impact of lanthanum and boron on the growth, thermomechanical properties and oxidation resistance of Ti–Al–N thin films, *Thin Solid Films* 688 (2019) <https://doi.org/10.1016/j.tsf.2019.04.014>.
- [57] T.A. Parthasarathy, M.G. Mendiratta, D.M. Dimiduk, Oxidation mechanisms in Mo-reinforced Mo₅SiB₂(T₂)-Mo₃Si alloys, *Acta Mater.* 50 (2002) 1857–1868, [https://doi.org/10.1016/S1359-6454\(02\)00039-3](https://doi.org/10.1016/S1359-6454(02)00039-3).